

Impacts of T-type intersections on the connectivity and flow in Complex two-dimensional fracture networks

Weiwei Zhu^a, Zhiqiang Chen^b, Yafan Yang^c, Wenbo Gong^a, Moran Wang^{a,*}

^a Department of Engineering Mechanics, Tsinghua University, Beijing, China

^b Petroleum Exploration and Production Research Institute, SINOPEC, Beijing, China

^c State Key Laboratory for Geomechanics and Deep Underground Engineering, China University of Mining and Technology, Xuzhou, China

ARTICLE INFO

Keywords:

T-type intersections
Connectivity
Permeability
Fracture growth
Stochastic discrete fracture networks

ABSTRACT

Natural fractures usually form T-type intersections, but the impacts of T-type intersections on the connectivity and flow results (such as permeability and fluid production) in complex fracture networks are rarely investigated. Here, a stochastic discrete fracture network method is implemented to construct complex two-dimensional fracture networks, denoted as original fracture networks. By implementing the rule-based fracture growth algorithm, the corresponding kinematic fracture networks are generated with a substantial proportion of T-type intersections. The connectivity and flow results of both the single-phase and two-phase flow simulations in these two types of fracture networks are systematically investigated. The results show that kinematic fracture networks tend to connect more fractures with fewer intersections and yield better connectivity than the original ones. Most kinematic fracture networks have larger permeability in the single-phase flow simulation and higher cumulative gas production in the two-phase flow simulation than original fracture networks under the same boundary conditions. The proportions of permeability and production enhancement are 68% and 77%, respectively. Flow results have strong positive correlations with the connectivity of fracture networks, but they are nonequivalent and strongly impacted by the number of inlets and outlets.

1. Introduction

Fractures provide essential pathways to subsurface flow in formations with low permeability (Berkowitz, 2002; Jeanpert et al., 2019; Laubach et al., 2019). However, available methods, including outcrop observations, wellbore logging, seismic mapping, and crosswell seismic techniques (Chesnaux et al., 2009; Ellefsen et al., 2002; Prioul and Jocker, 2009; Rijks and Jauffred, 1991; Ukar et al., 2019; Wilt et al., 1995), are insufficient to have detailed characterizations of subsurface fracture networks. Stochastic discrete fracture networks (SDFNs) are a practical alternative to describe subsurface fractures by preserving main geometrical properties, such as fracture lengths, center positions, orientations, and topological structures, but neglecting intricate details, like fracture roughness and curved shapes. SDFNs are widely used to investigate the natural fracture networks and their impact on the subsurface flow (Bour and Davy, 1997a, 1998; Koudina et al., 1998; Lei et al., 2017; Mourzenko et al., 2011; Wang et al., 2007; Xiong et al., 2022).

The ordinary procedure to generate SDFNs includes: i, choosing a

generation volume; ii, choosing proper statistical distributions to describe fracture geometries; iii, generating discrete fractures according to the chosen distributions in succession; iv, stopping generating fractures when the termination criterion is reached, such as a prescribed fracture intensity. Through implementing the procedure, it is almost impossible to generate fractures abutting the other fractures (T-type intersections, Fig. 1a), and only cross fractures (X-type intersections, Fig. 1b) are available. However, it is common to observe T-type intersections in real outcrop maps, which take a significant proportion of the total intersections (Dershowitz and Einstein, 1988; Watkins et al., 2015; Zhu et al., 2022b). Fig. 2 presents two examples of fracture outcrop maps, and different types of nodes are marked in different colors. The proportions of T-type intersections are 74% and 76%, respectively. V-type intersections (Fig. 1c) have coincident tips and are unlikely to form in reality (Sanderson and Nixon, 2015), which are not distinguished from T-type intersections in Fig. 2.

T-type intersections are naturally formed during the fracture growth process, and they are important to enhance the connectivity of fracture networks because of the reduction of dead-ends (Barton and Hsieh,

* Corresponding author.

E-mail address: mrwang@tsinghua.edu.cn (M. Wang).

<https://doi.org/10.1016/j.enggeo.2023.107122>

Received 23 August 2022; Received in revised form 3 December 2022; Accepted 19 April 2023

Available online 23 April 2023

0013-7952/© 2023 Elsevier B.V. All rights reserved.

1989; Odling, 1997). Complex numerical schemes are necessary to obtain the accurate stress/strain field considering different rock types, strengths, and stress states (Chen and Wang, 2017; Olson et al., 2009). However, in complex fracture networks, such numerical simulation is computationally unacceptable. Therefore, detailed investigations on the impact of T-type intersections on the connectivity and subsurface flow in complex fracture networks are rarely conducted.

Davy et al. (2013, 2010) considered the fracture growth process by simplifying the complex mechanical calculation with three steps: nucleation, growth, and arrest. The method provides different constraining rules according to field and experiment observations and mechanical principles, which renders main mechanical interactions and forms many T-type intersections. A similar method is adopted by Bonneau et al. (2013) to consider fracture coalescence and its impacts on connectivity. Maillot et al. (2016) implemented the nucleation-growth-arrest method and investigated the impact of T-type intersections on fracture connectivity and flow, where meaningful findings and conclusions were summarized. However, their cases are limited to comparisons between the kinematic and Poisson models, where fracture centers and fracture orientations are uniformly distributed. Percolation analysis was involved, but the conventional percolation threshold derived from the excluded volume method is only applicable to the Poisson model dominated by small fractures (Bour and Davy, 1997a; Zhu et al., 2018). Natural fractures are usually spatially clustered instead of uniform (Akara et al., 2021; Zhu et al., 2018) and preferential orientations depending on stress history are commonly observed (Kemeny and Post, 2003; Laubach, 1988; Watkins et al., 2015). Therefore, a more systematic analysis regarding complex fracture networks is necessary to investigate the impact of T-type intersections on the connectivity and subsurface flow.

In this work, the rule-based nucleation-growth-arrest method is adopted to generate T-type intersections in complex two-dimensional fracture networks, considering a wide range of geometrical variations on fractures. In specific, different levels of fracture lengths, orientations, and clustering degrees are considered. Two types of fracture networks are constructed for comparison: original (no fracture growth algorithm implemented) and kinematic fracture networks (with fracture growth algorithm implemented). The impacts of T-type intersections on the connectivity and subsurface flow are then systematically investigated.

The paper is organized as follows: Section 2 introduces techniques to construct complex fracture networks and generate T-type intersections. Topology analysis and flow simulation details are also included in Section 2. Section 3 presents the results of the systematic analysis of two types of fracture networks. The impact of T-type intersections on the connectivity and subsurface flow is analyzed in detail. Limitations and possible improvements are presented in Section 4. Section 5 summarizes important findings and conclusions.

2. Materials and methods

This section introduces techniques to construct complex fracture networks and their corresponding kinematic fracture networks considering the fracture growth process. Detailed information for the single and two-phase flow simulation is also presented.

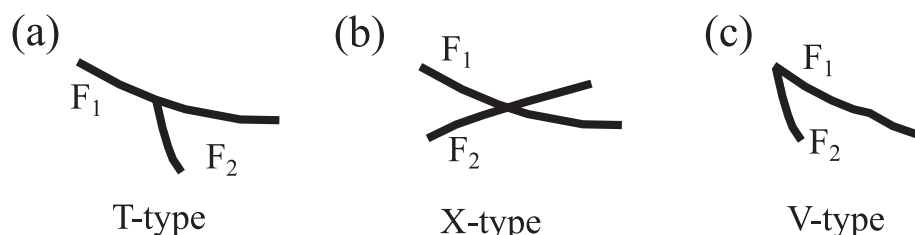


Fig. 1. Demonstration of different types of intersections between fractures. F_1 and F_2 refer to the first and second fracture.

2.1. Fracture network construction and topology analysis

The process to construct discrete fracture networks is intensively discussed in our recent work on DFN modeling software, HatchFrac (Zhu et al., 2022c). This work considers three main geometrical properties of fractures, and each property is described by a different statistical distribution. A power-law distribution is adopted to describe fracture length (Bour and Davy, 1997b). The fracture orientations are characterized by a von Mises-Fisher distribution (Whitaker and Engelder, 2005). The fractal spatial density distribution is implemented to generate clustered fracture centers, which is closer to the reality (Akara et al., 2021; Zhu et al., 2022b). A fractal dimension characterizes the fractal spatial density distribution and varies between 1.0 and 2.0 for fracture networks in 2D. The system size is 100 arbitrary units, and the minimum length of fractures is 10 units. From outcrop observations, the exponent of the power-law usually varies in the range of [2.0, 3.0] (Bonnet et al., 2001; Zhu et al., 2018) and the concentration parameter κ is usually smaller than 3.0 for networks composed of several fracture sets (Zhu et al., 2022b). In this work, three levels of each parameter are chosen to represent different scenarios of complex fracture networks. A Taguchi method (Karna et al., 2012) is adopted to generate nine orthogonal cases with three levels for three parameters. 10 independent realizations of each case are generated to avoid random effects from statistical distributions, and in total, there are 90 realizations analyzed in this work. Although the analysis of the 2D fracture network is emphasized here, similar procedures can be applied to 3D fracture networks. Table 1 summarizes the parameters for each case.

After choosing the parameters for different statistical distributions, the discrete fracture network can be constructed by adding fractures in succession. The termination criterion is when the fracture network is over-percolative, where the fracture intensity is twice as large as the intensity at the percolation state. The over-percolative state (a state where the fracture intensity is larger than the intensity at percolation) is widely observed from natural outcrops (Watkins et al., 2015; Zhu et al., 2022d). Fracture networks with and without considering fracture growth are denoted as original and kinematic fracture networks, respectively.

Connectivity determines the hydraulic diffusivity of a fracture network and significantly impacts the flow behavior. Several methods are available to measure the connectivity of the fracture system, such as the percolation analysis (Bour and Davy, 1997b; Huseby et al., 1997; Thovert et al., 2017), the connectivity index/field method (Fadakar-A et al., 2013; Xu et al., 2006), global efficiency method (Zhu et al., 2021), and ternary diagram method (Barton and Hsieh, 1989). In this work, aperture variations of fractures are not included. Therefore, a topological measure, C_B , the mean number of linkages of each branch, is sufficient and convenient to evaluate the fracture network connectivity (Sanderson and Nixon, 2015).

$$C_B = \frac{4N_X + 3N_T}{N_B}, \quad (1)$$

where N_T , N_X , and N_B refer to the numbers of T-type nodes, X-type nodes, and branches. N_B is calculated by:

$$N_B = \frac{1}{2}(N_I + 3N_T + 4N_X), \quad (2)$$

where N_I refers to the number of I-type nodes.

C_B is dimensionless and varies between 0 and 2.0, where better connectivity yields a larger value. The topology analysis and connectivity index calculation are conducted for the largest cluster of the fracture network (red fractures in Fig. 3) instead of all fractures because the subsurface fluid flows through well-connected fracture networks instead of isolated fractures in formations with low permeability.

Figs. 3(a) and (b) show two examples of original fracture networks with different combinations of geometrical parameters. The fracture network in Fig. 3(a) has $a = 3.0$, $F_D = 2.0$, and $\kappa = 5.0$. The total amount of intersections in the largest fracture cluster is 1210. The connectivity index is 1.724. The fracture network in Fig. 3(b) has $a = 2.0$, $F_D = 1.5$, and $\kappa = 0$. The total number of intersections and the connectivity index of the largest cluster are 522 and 1.80, respectively.

2.2. Fracture growth and T-type intersections

The rule-based fracture growth algorithm constrains the growth process with specific nucleation, growth, and arrest rules. Making original and kinematic fracture networks similar is essential to compare the impacts of T-type intersections on connectivity and flow results. To this effect, we construct a corresponding kinematic counterpart for each original fracture network. The number of nuclei equals the number of fractures in the original fracture network. Each nucleus grows in the same direction as the original fracture. Therefore, P_{20} (the number of fractures per unit area) and the orientation distribution are the same for the original and kinematic fracture networks.

Furthermore, the fracture intensity, P_{21} (the length of fracture traces per unit area), is set the same for the original and kinematic fracture networks. The kinematic fracture network requires one degree of freedom to match the prescribed intensity. Fracture lengths, depending on the velocity model and arrest criterion, are convenient to be adjusted in kinematic fracture networks to match the intensity. The arrest criterion implemented is that each fracture tip stops growing when it encounters a large fracture (Davy et al., 2010; Nur, 1982; Segall and Pollard, 1983). The growth velocity at fracture tips follows a power-law distribution if fracture propagation happens in a stable and quantifiable sub-critical regime (Engelder, 2004; Olson, 2004).

$$v = dl/dt = A \left(\frac{K_I}{K_{IC}} \right)^n \quad (3)$$

where K_I is a stress intensity factor of the opening mode at the fracture tip; K_{IC} is the fracture toughness at the opening mode; A is a proportionality coefficient; n is a sub-critical growth index of the fracture, depending on environmental conditions and rock types. $n = 0$ is chosen in this work, but the other values corresponding to specific rock types and environmental conditions can be implemented without difficulty. Therefore, the growth velocity considered is a constant, and the growth

Table 1
Parameters for complex fracture networks.

Parameter	Low	Intermediate	High	Definition
Fracture length, a	2.0	2.5	3.0	The exponent of a power-law distribution
Position of the fracture center, F_D	1.5	1.7	2.0	The fractal dimension of a fractal spatial density distribution
Fracture orientation, κ	0	5	10	The concentration parameter in a von Mises-Fisher distribution

velocity of the i^{th} fracture is set as a combination of a constant part and a length-related random part, which yields one degree of freedom to match the P_{21} value.

$$v_i = l_c + \text{rand} \left(0, \beta \times \frac{l_i}{l_{max}} \right) \quad (4)$$

where l_c is the constant velocity for all fractures and set as 5 units/step; $\text{rand}(a, b)$ is a function to generate random variables distributed in the interval $[a, b]$; β is a constant weight to adjust the growth velocity and set as 2.0; l_i is the length of original fracture; l_{max} is the largest fracture length in the original fracture network.

Eq. 4 provides a degree of freedom with the random function to match the prescribed fracture intensity. Furthermore, larger fractures in the original fracture network tend to have a higher growth velocity and remain in a similar shape in the kinematic fracture network. Choices of l_c and β are determined with trial and error to ensure the chosen combination can reach convergence efficiently.

Figs. 3(c) and (d) show the corresponding kinematic fracture networks of Figs. 3(a) and (b). The total number of intersections in the largest fracture cluster of the fracture network in Fig. 3(c) is 1150, and the connectivity index is 1.827. For the fracture network in Fig. 3(d), the total number of intersections and the connectivity index of the largest cluster are 450 and 1.877, respectively.

2.3. Single/two-phase flow simulation

The single-phase and two-phase flow are essential for real engineering applications and the impact of T-type intersections are thoroughly investigated. The enhanced geothermal extraction process is a typical simplified single-phase flow example, where cold water is injected into the subsurface formation and transported to the production well through the fracture network. A two-phase flow simulation can mimic the simplified process of shale gas production, where natural gas stored in the matrix first flows to the fracture network and then to the production well. The single/two-phase flow simulation is conducted with UNCONG, where embedded discrete fracture network techniques are adopted and detailed technical information is available in the reference (Li et al., 2015). In the flow simulation, the unit of the system size is chosen as a meter for convenient calculations.

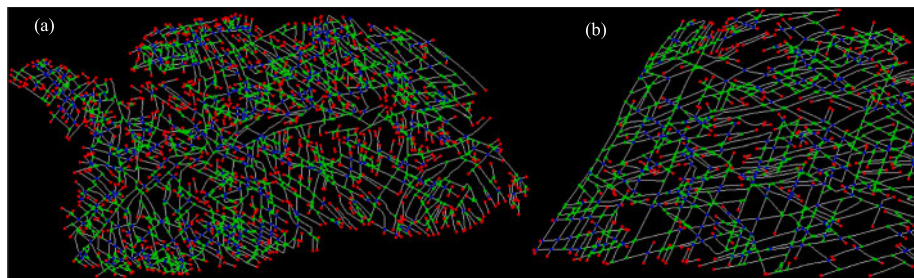


Fig. 2. Fracture outcrop map at Achnashellach Culmination field area in North-West Scotland (Figs. 7(B,D) in Watkins et al. (2015)) with different types of intersection nodes marked in different colors. Red nodes are isolated nodes; Green nodes refer to T-type intersection nodes; Blue nodes represent X-type intersection nodes. (For interpretation of the references to colour in this figure legend, the reader is referred to the web version of this article.)

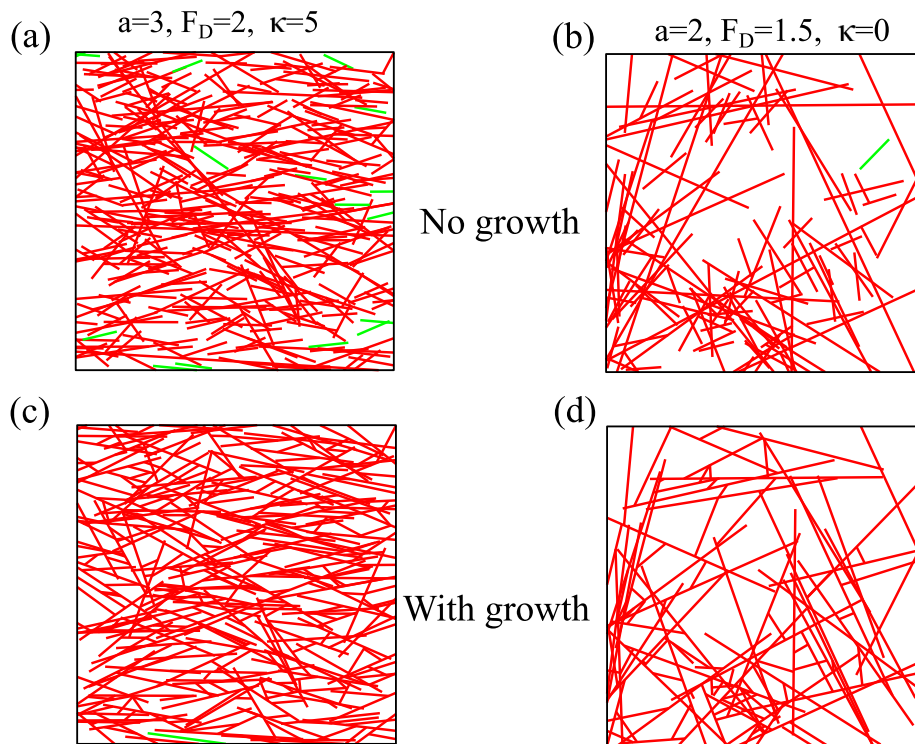


Fig. 3. Examples of the original fracture networks (a, b) and the corresponding kinematic fracture networks (c,d). Red line segments refer to the largest fracture cluster and green line segments are isolated clusters. (For interpretation of the references to colour in this figure legend, the reader is referred to the web version of this article.)

For the single-phase flow simulation, the matrix is assumed to be impermeable and constant pressure boundary conditions are implemented for all fracture networks. A constant pressure of 200 kPa is assigned to the inlet boundary (left side). 0 kPa is assigned to the outlet boundary (right side). The chosen pressure values constrict the Reynolds number to a feasible range, $\mathcal{O}(10^{-3})$, and yield a pressure gradient of 2.0 kPa/m (Zhu et al., 2021). The top and bottom boundaries are set impermeable. A sketch map of the boundary condition for the single-phase flow is demonstrated in Fig. 4(a). Fig. 5(a) presents the pressure distribution of the single-phase flow in the fracture network (Fig. 3(a)). UNCONG treats all fractures as 3D objects. Therefore, 2D fracture networks are represented as 3D fracture networks with a constant height.

For the two-phase flow, we consider the gas-water flow in formations with ultra-low permeability. The matrix's permeability is set as 1.0 micro-darcy. Fractures have a high permeability of 10 darcies, seven orders of magnitude higher than the matrix permeability. The initial formation pressure is set as 30,000 kPa. A horizontal well is drilled at the

middle of the formation, and the bottom-hole pressure is set as 10,000 kPa and kept constant. Fig. 4(b) presents a sketch map of the boundary condition for the two-phase flow. Detailed input parameters are listed in Table 2. Fig. 6(a) shows the compressibility and viscosity changes of gas with pressure. The relative permeability curves adopted for the two-phase flow simulation in the matrix and fracture are shown in Figs. 6 (b) and (c), respectively. The production is simulated for ten days considering the computational cost and Fig. 5(b) shows the pressure distribution in the formation after the production.

3. Results

The corresponding kinematic fracture networks share the same orientations and fracture intensities, both P_{20} and P_{21} , as the original fracture networks. However, 87 out of 90 kinematic fracture networks show different length distributions from the original ones based on a Two-sample Kolmogorov-Smirnov test, which is necessary to match the prescribed fracture intensity.

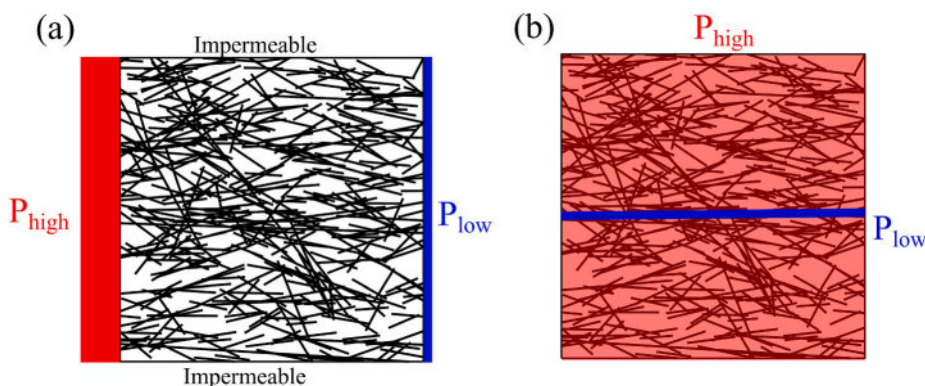


Fig. 4. Boundary conditions for the single-phase (a) and two-phase (b) flow.

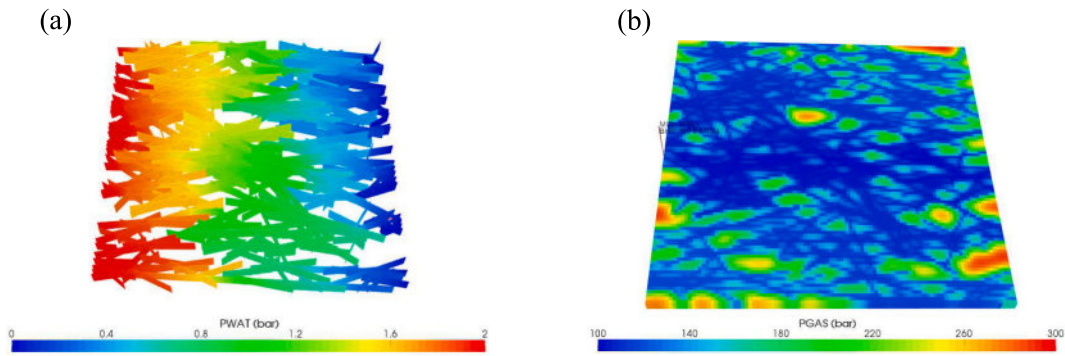


Fig. 5. Pressure distribution in the single-phase flow simulation (a) and two-phase flow simulation (b).

Table 2

Input parameters for the two-phase simulation.

Property	Value
Matrix permeability, k_m [μd]	1.0
Matrix porosity, ϕ_m [-]	0.05
Fracture permeability, k_f [d]	10
Fracture porosity, ϕ_f [-]	1.0
Water compressibility coefficient, B_w [kPa^{-1}]	$3.15e-4$
Water viscosity compressibility coefficient, $B\mu_w$ [$cP \cdot kPa^{-1}$]	$2.10e-4$
Initial water saturation, S_{wi} [-]	0.5
Initial formation pressure, P_i [kPa]	30,000
Bottomhole pressure, P_b [kPa]	10,000

Fig. 7 shows the proportion of T-type intersections out of total intersections. Almost no T-type intersections exist in the original fracture networks, and the corresponding proportion is close to zero for all scenarios (blue circles). After implementing the fracture growth algorithm, the proportion of T-type intersections is significantly increased (red circles), and the mean proportion of the 90 scenarios is 0.32.

Fig. 8 shows the ratio of the total number/ length of fractures in the largest cluster and the whole domain in both kinematic and original fracture networks. Green line segments linking two fracture networks represent an increase from the original case to the corresponding kinematic case, and black line segments denote a decrease. All cases have more fractures belonging to the largest cluster in the kinematic fracture networks than the original ones. 4 out of 90 cases have larger fracture lengths in the original fracture networks than in the kinematic ones. Fig. 9 shows the ratios of total intersections and connectivity index between the kinematic and original fracture networks. Most cases have better connectivity in the kinematic than the original fracture networks. The only different case also has its connectivity index ratio close to 1.0. Most of the scenarios (77 out of 90) have fewer intersections in the kinematic than the original fracture networks. The decreasing

intersections and increasing fracture numbers yield a decreasing intersection per fracture (I_{pf}) in the kinematic fracture networks. I_{pf} has been adopted as a percolation parameter and a measure of connectivity for fracture networks with constant fracture lengths and uniformly distributed fracture centers and orientations (Robinson, 1983). However, the results here demonstrate that I_{pf} is an invalid parameter to characterize the connectivity of complex fracture networks as concluded by Bour and Davy (1998) and Zhu et al. (2018). In a kinematic fracture network with substantial T-type intersections, the connectivity is enhanced, and more fractures are connected to form a larger cluster, but the number of intersections usually decreases.

From the single-phase flow simulation, the permeability of the fracture network is calculated. Fig. 10 shows the ratio of permeability between kinematic and original fracture networks. Out of 90 cases, 61 cases have their permeability increased in the kinematic fracture networks compared with the original ones. The maximum increase of permeability can be 3.5 times. Different fracture geometries (fracture length, positions, and orientations) have a different impact on the permeability ratio. Therefore, results are plotted separately in different colors and sub-figures regarding fracture length (a), positions of fracture centers (F_D), and concentrated fracture orientations (κ). The number of cases with a permeability ratio larger than 1.0 is denoted in the figure. From Fig. 10 (a), more cases have a higher permeability in the kinematic fracture networks with an increase of a , indicating that kinematic fracture networks composed of small fractures tend to have higher permeability. The clustering effects have a positive contribution to the permeability enhancement in the kinematic fracture networks, as shown in Fig. 10 (b). Fig. 10 (c) shows non-monotonic variations of concentrated fracture orientations on the permeability ratio, indicating an insignificant impact from the orientation concentration on the permeability enhancement.

An input/output correlation method is implemented to evaluate the impact of each independent geometrical parameter on the permeability

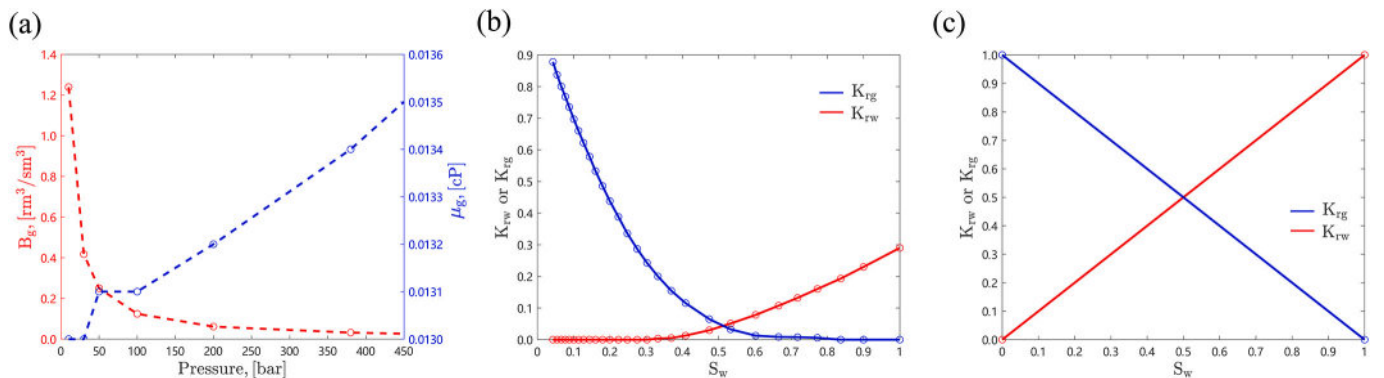


Fig. 6. (a) the compressibility (B_g) and viscosity (μ_g) changes of gas with pressure; (b) the relative permeability curve for the two-phase flow simulation in the matrix; (c) the relative permeability curve for the two-phases flow simulation in fractures; After Zhu et al. (2022a).

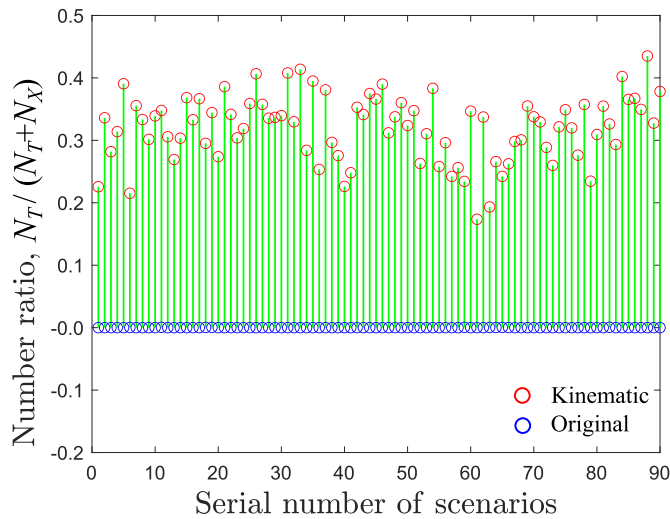


Fig. 7. The ratio between the number of T-type intersections (N_T) and total intersections (T-type, N_T plus X-type, N_X).

of kinematic and original fracture networks. The sensitivity of each parameter is measured according to the correlation coefficient, ρ , between the parameter and the response. Fig. 11 shows the sensitivity

analysis of fracture geometries with different responses, including the permeability of original fracture networks (Fig. 11a), the permeability of kinematic fracture networks (Fig. 11b), and the permeability ratio between these two types of fracture networks (Fig. 11c). For the original and kinematic fracture networks, both a and κ have positive correlations with the permeability, indicating that fracture networks composed of small fractures with concentrated orientations tend to have higher permeability. The orientation concentration has a more critical impact on permeability enhancement. F_D has slightly negative correlations, indicating that clustering effects can enhance permeability and this effect is more significant in kinematics fracture networks. a and F_D have positive and negative correlations with the permeability ratio. κ has an insignificant impact on the permeability ratio. The correlation results in Fig. 11(c) are consistent with behaviors shown in Fig. 10.

Fig. 12 shows ratios of cumulative gas production after ten days between kinematic and original fracture networks. In all 90 cases, 69 cases have their cumulative production larger in the kinematic fracture networks than in the original ones. The maximum increase can be 1.4 times. Different sub-figures and colors are presented for different geometrical parameters (a , F_D , and κ). a and F_D have positive and negative impacts on the production ratio, similar to the results in the permeability ratio in Figs. 10(a, b). Therefore, kinematic fracture networks that are composed of small fractures (a larger exponent, a) with strong clustering effects (a smaller fractal dimension, F_D) tend to produce more than the original ones. The concentration parameter κ has a

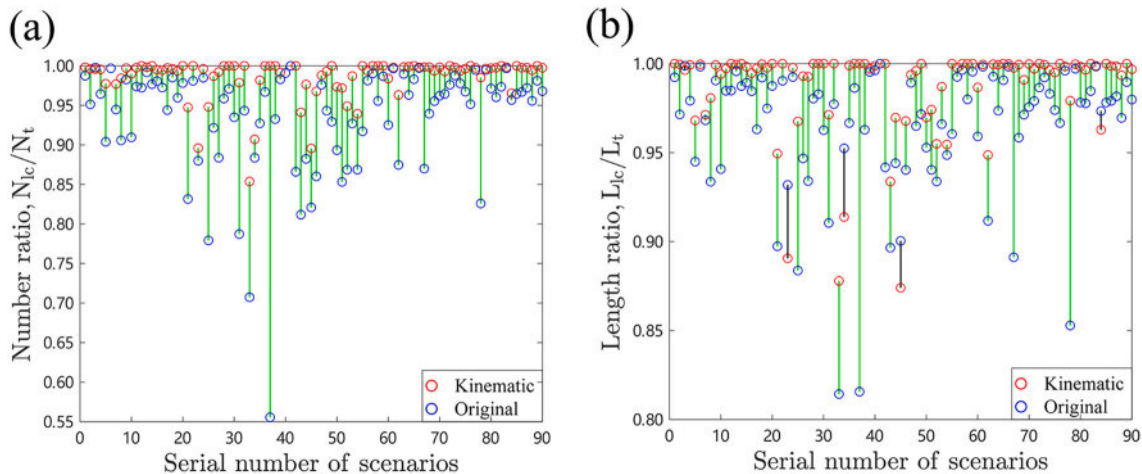


Fig. 8. Ratios between the number (a) and length (b) of fractures in the largest cluster (N_{lc} , L_{lc}) and the number and length of total fractures (N_t , L_t).

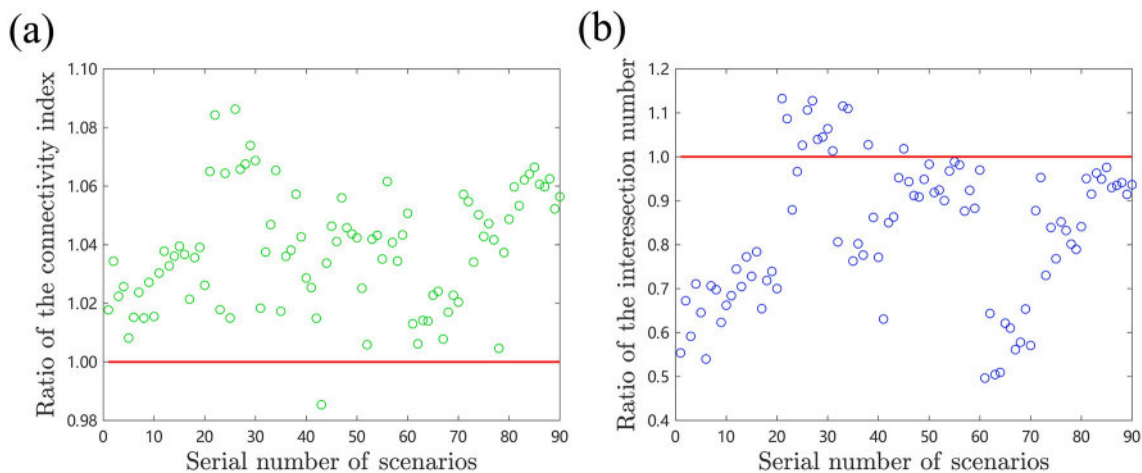


Fig. 9. Ratios of the connectivity index (a) and the total number of intersections (b) between the kinematic and original fracture networks.

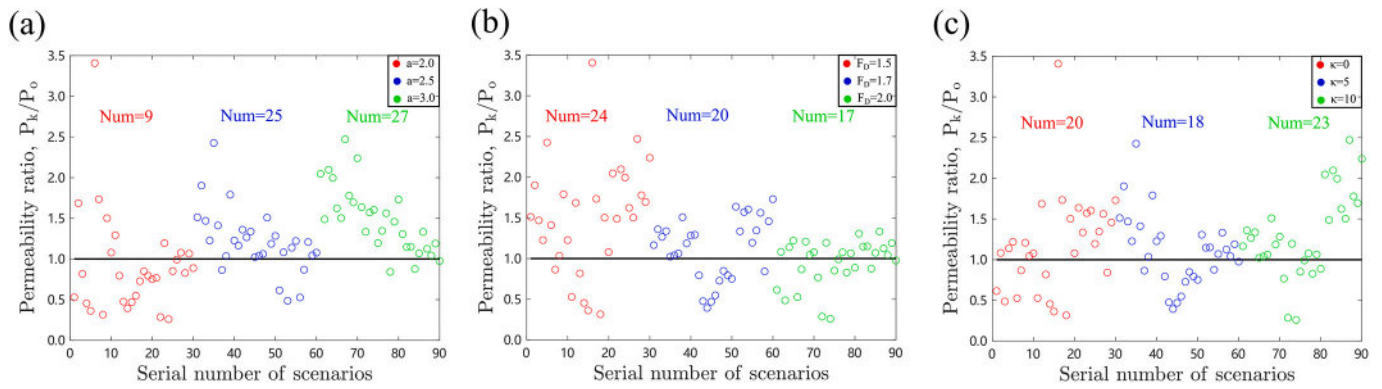


Fig. 10. Permeability ratio between the kinematic fracture networks and the original ones. Different sub-figures classify the permeability ratio based on the geometrical parameters: (a) the power-law exponent α ; (b) the fractal dimension F_D ; (c) the concentration parameter κ . The number of cases with a ratio larger than 1.0 is denoted.

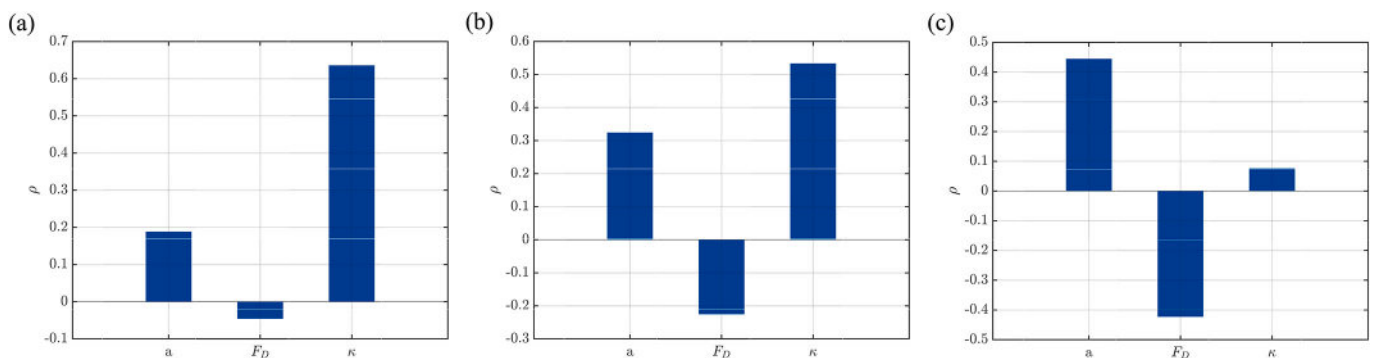


Fig. 11. Sensitivity analysis of fracture geometries with, (a) permeability of origin fracture networks; (b) permeability of kinematic fracture networks; (c) permeability ratio between kinematic and original fracture networks, as responses. ρ is the correlation coefficient between the parameter and the response.

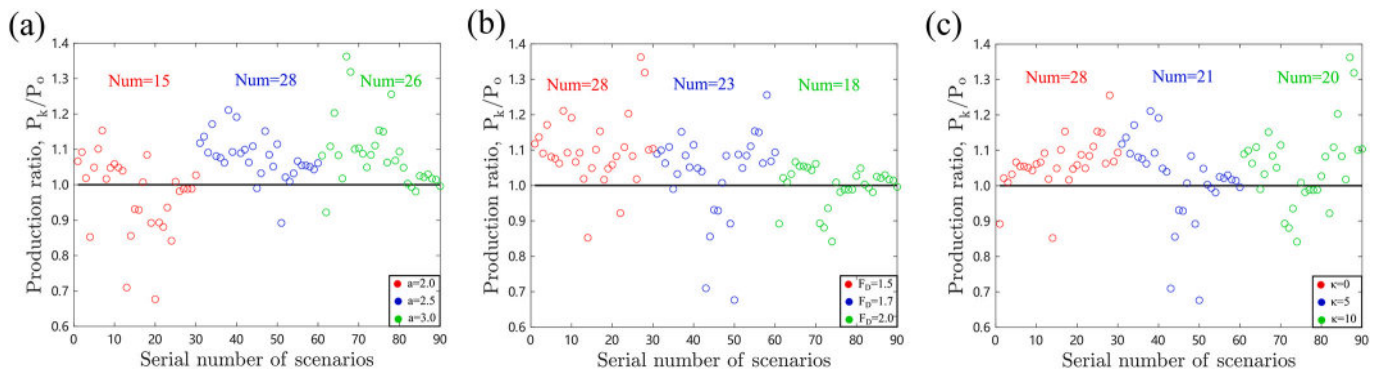


Fig. 12. Production ratio between the kinematic fracture networks and the original ones. Different sub-figures classify the production ratio based on the geometrical parameters: (a) the power-law exponent α ; (b) the fractal dimension F_D ; (c) the concentration parameter κ . The number of cases with a ratio larger than 1.0 is denoted.

negative impact on the production ratio instead of non-monotonic variations shown in Fig. 10(c), indicating that concentrated fracture orientations may not help to enhance production in kinematic fracture networks.

Fig. 13 shows similar sensitivity analyses with different responses, including the cumulative gas production from original and kinematic fracture networks and the production ratio between these two types of fracture networks. Compared with the sensitivity results on permeability in Fig. 11, the exponent α and concentration parameter κ have similar results, positive correlations with the cumulative gas production in both kinematic and original fracture networks. However, the fractal dimension F_D has a positive correlation, indicating that clustering effects cannot increase gas production, and this impact is more significant in

the original fracture networks. In Fig. 13(c), the sensitivity results are consistent with the observations in Fig. 12 with a positive correlation for α , a negative correlation for F_D and a weak negative correlation for κ .

Most kinematic fracture networks have higher permeability or cumulative gas production than original ones, and the corresponding proportions are 68% and 77%, respectively. However, the percentage of cases with a connectivity enhancement in kinematic fracture networks is almost 100%. Therefore, flow behaviors and connectivity of fracture networks are correlated but nonequivalent, and flow results are not good candidates to evaluate the connectivity of complex fracture networks as discussed by Zhu et al. (2021). The flow behaviors, such as permeability or fluid production, can be affected by the other geometrical configurations and different boundary conditions. Here, the impact of the

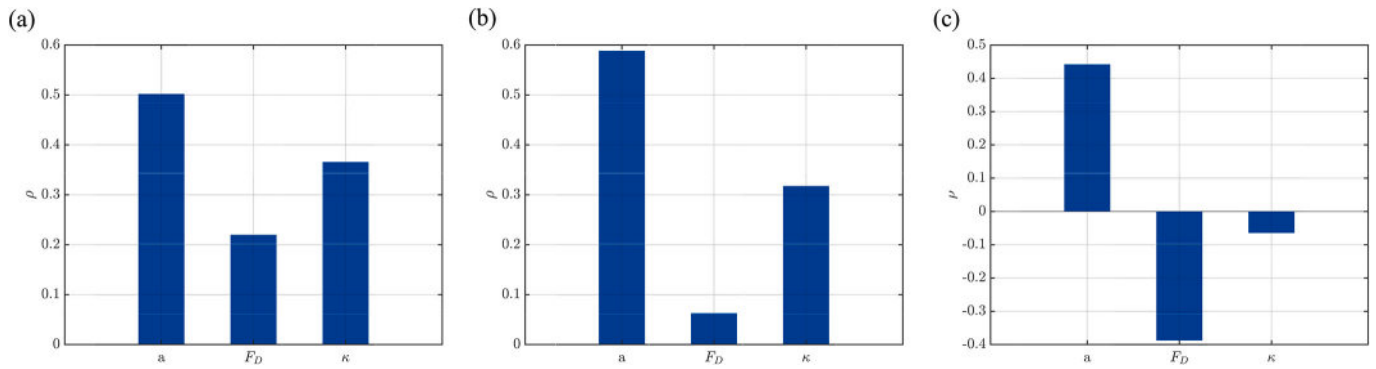


Fig. 13. Sensitivity analysis of fracture geometries with, (a) cumulative gas production from origin fracture networks; (b) cumulative gas production from growth fracture networks; (c) cumulative gas production ratio between origin and growth fracture networks, as responses. ρ is the correlation coefficient between the parameter and the response.

number of inlets and outlets is investigated with available data. For single-phase flow, the number of inlets and outlets is the number of fractures intersecting the left and right boundaries. All fractures serve as inlet fractures for the two-phase flow, and the outlets are fractures intersecting the production well in the middle of the formation.

The correlations are summarized in Table 3. Possible influential parameters in both kinematic and original fracture networks include the number of inlets and outlets for the single-phase flow, the number of outlets for the two-phase flow, and the connectivity index. The responses include the permeability of kinematic and original fracture networks, the cumulative gas production from kinematic and original fracture networks, and the ratios of permeability and cumulative production of these two types of fracture networks.

The parameters listed in Table 3 are not included in the sensitivity analysis of geometrical parameters because they are not independent of each other. For example, the number of inlets/outlets depends on the connectivity index, which correlates with geometrical parameters (a , F_D , and κ). From the correlation coefficients shown in Table 3, the connectivity index has a positive correlation with flow results, including the permeability and cumulative production, indicating better connectivity of a fracture network can lead to better flow performance. However, the number of inlets/outlets is also strongly correlated with the flow results, even with a higher correlation coefficient than the connectivity index. For the permeability calculation in the original fracture networks, the correlation coefficients of the number of inlets/outlets are 0.78 and 0.90, respectively. In the kinematic fracture networks, the correlation coefficients are 0.97 for both the number of inlets and outlets. For the cumulative production, the correlations between the number of outlets and cumulative production from the original and kinematic fracture networks are 0.74 and 0.69, respectively. Although the impact of inlets/outlets is not directly comparable with geometrical parameters, it is still qualitatively correct to conclude that the number of inlets and outlets significantly impacts the flow results. The impact of inlets/outlets on the

permeability and production ratios is not as significant as the impact on individual permeability and production. Instead, the connectivity index correlates relatively better with permeability and production ratios.

4. Discussion

From a massive collection of outcrop maps, Zhu et al. (2022b) calculated different types of intersections in 80 natural fracture networks and plotted the proportion of each type of node in a ternary diagram (Fig. 14). They found that most natural fracture networks have a large proportion of T-type intersections. Therefore, T-type intersections are commonly formed in natural fractures.

This work chooses the SDFN method to construct complex fracture networks instead of using natural outcrop maps because with SDFN, it is more convenient to construct fracture networks with systematic patterns and we can evaluate the impact of each fracture geometrical pattern on the formation of T-type intersections and fluid flow. Furthermore, the comparison between the original and kinematic fracture networks and emphasizing the impact of T-type intersections are possible with the SDFN method because we can constrain the fracture orientations and intensities to make two fracture networks as similar as possible. However, in real outcrop maps, it is difficult to construct a similar counterpart fracture network with no T-type intersections.

It is necessary to have detailed numerical simulations to investigate the formation of T-type intersections considering the global stresses and interactions of neighboring fractures. Specific rules of fracture growth can be further implemented into complex discrete fracture networks to constrain the kinematic fracture networks and make them closer to reality. For example, multiple fracture sets with preferential orientations can be generated considering different stress states, which is commonly observed from outcrop maps.

In addition, the fracture permeability is set constant in this work, while natural fractures have various apertures due to significant

Table 3
Correlation coefficients between different parameters and responses.

Response Parameter	Permeability (Original)	Permeability (Kinematic)	Ratio of permeability	Cumulative production (Original)	Cumulative production (Kinematic)	Ratio of production
No. inlets ^{SP} (Original)	0.78	–	0.49	–	–	–
No. inlets ^{SP} (Kinematic)	–	0.97	0.48	–	–	–
No. outlets ^{SP} (Original)	0.90	–	0.10	–	–	–
No. outlets ^{SP} (Kinematic)	–	0.97	0.37	–	–	–
No. outlets ^{TP} (Original)	–	–	–	0.74	–	0.16
No. outlets ^{TP} (Kinematic)	–	–	–	–	0.69	0.30
Connectivity index (Original)	0.61	–	0.71	0.65	–	0.58
Connectivity index (Kinematic)	–	0.63	0.67	–	0.85	0.54

SP: single-phase flow simulation; TP: two-phase flow simulation.

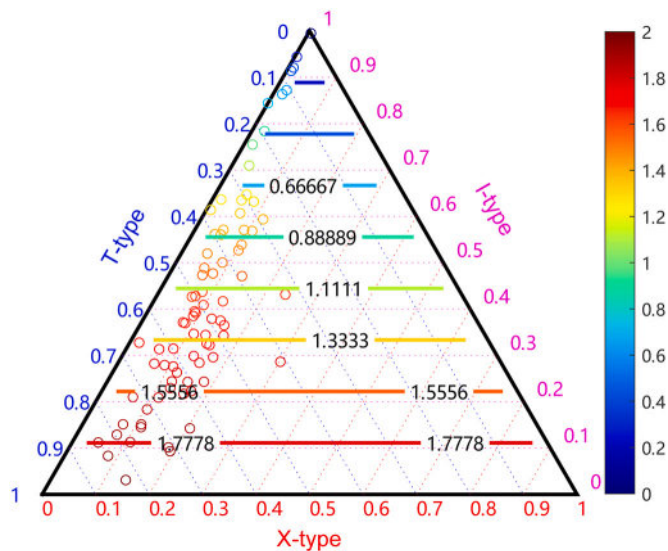


Fig. 14. Ternary diagram of three types of nodes in 80 collected natural fracture outcrop. After Zhu et al. (2022b).

compression and cementation (Im et al., 2018). Actual flow conditions can be extremely complicated considering complex fluid properties and various boundary conditions. However, considering the magnificent computational cost, we significantly simplify the flow simulation to emphasize the topological structure of fractures and systematically investigate the impact of T-type intersections in a relatively simple system. More in-depth research is needed in the future, considering physical constraints on the fracture growth process, complex fracture systems composed of multiple fracture sets, various fracture apertures, and different boundary conditions.

5. Conclusions

In this work, we construct complex fracture networks with their main geometries (fracture lengths, orientations, and center positions) constrained by different statistical distributions. Multiple levels of geometrical parameters are chosen to make generated fracture networks more representative. By implementing the rule-based fracture growth method, we construct the corresponding kinematic fracture networks, which share the same fracture orientations and fracture intensities (P_{20} and P_{21}) as the original fracture networks. Connectivity and flow results in the original and kinematic fracture networks are systematically analyzed, and several essential conclusions are summarized:

- Kinematic fracture networks tend to connect more fractures with fewer intersections compared with the original fracture networks.
- Kinematic fracture networks systematically have better connectivity than the original fracture networks.
- Most kinematic fracture networks have larger permeability in the single-phase flow simulation and higher cumulative gas production in the two-phase flow simulation than original fracture networks under the same boundary conditions. The proportions of permeability and production enhancement are 68% and 77%, respectively.
- Flow results, like the permeability and production, have strong positive correlations with the connectivity of fracture networks, but they are nonequivalent and strongly impacted by the number of inlets and outlets.

CRedit authorship contribution statement

Weiwei Zhu: Conceptualization, Methodology, Investigation, Writing – original draft. **Zhiqiang Chen:** Investigation, Writing –

original draft, Resources. **Yafan Yang:** Investigation, Resources. **Wenbo Gong:** Investigation, Data curation, Visualization. **Moran Wang:** Conceptualization, Supervision, Writing – review & editing, Project administration, Funding acquisition.

Declaration of Competing Interest

The authors declare that they have no known competing financial interests or personal relationships that could have appeared to influence the work reported in this paper.

Data availability

The original and kinematic fracture networks are generated by an in-house DFN modeling software, HatchFrac. Detailed information about the software can be found at Zhu et al. (2022c). The C++ code for generating 2D and 3D fracture networks and simulating the fracture growth process is available online (<https://data.mendeley.com/datasets/zhs97tsdry/1>).

Acknowledgments

This project was supported by the National Key Research and Development Program of China (No. 2019YFA0708704). The authors would like to thank Dr. X. Li from Ennosoft for providing the UNCONG simulator to simulate the single-phase and two-phase flow. The authors would like to thank all editors and anonymous reviewers for their comments and suggestions.

References

- Akara, M.E.M., Reeves, D.M., Parashar, R., 2021. Impact of horizontal spatial clustering in two-dimensional fracture networks on solute transport. *J. Hydrol.* 603, 127055.
- Barton, C., Hsieh, P., 1989. Physical and hydrologic-flow properties of fractures. In: 28th International Geological Congress Field Trip Guidebook, p. 36.
- Berkowitz, B., 2002. Characterizing flow and transport in fractured geological media: a review. *Adv. Water Resour.* 25, 861–884.
- Bonneau, F., Henrion, V., Caumon, G., Renard, P., Sausse, J., 2013. A methodology for pseudo-genetic stochastic modeling of discrete fracture networks. *Comput. Geosci.* 56, 12–22.
- Bonnet, E., Bour, O., Odling, N.E., Davy, P., Main, I., Cowie, P., Berkowitz, B., 2001. Scaling of fracture systems in geological media. *Rev. Geophys.* 39, 347–383.
- Bour, O., Davy, P., 1997a. Connectivity of random fault networks following a power law fault length distribution. *Water Resour. Res.* 33, 1567–1583.
- Bour, O., Davy, P., 1997b. Connectivity of random fault networks following a power law fault length distribution. *Water Resour. Res.* 33, 1567–1583.
- Bour, O., Davy, P., 1998. On the connectivity of three-dimensional fault networks. *Water Resour. Res.* 34, 2611–2622.
- Chen, Z., Wang, M., 2017. Pore-scale modeling of hydromechanical coupled mechanics in hydrofracturing process. *J. Geophys. Res. Solid Earth* 122, 3410–3429.
- Chesnaux, R., Allen, D., Jenni, S., 2009. Regional fracture network permeability using outcrop scale measurements. *Eng. Geol.* 108, 259–271.
- Davy, P., Le Goc, R., Darcel, C., Bour, O., De Dreuzy, J.R., Munier, R., 2010. A likely universal model of fracture scaling and its consequence for crustal hydromechanics. *J. Geophys. Res. Solid Earth* 115.
- Davy, P., Le Goc, R., Darcel, C., 2013. A model of fracture nucleation, growth and arrest, and consequences for fracture density and scaling. *J. Geophys. Res. Solid Earth* 118, 1393–1407.
- Dershowitz, W., Einstein, H., 1988. Characterizing rock joint geometry with joint system models. *Rock Mech. Rock. Eng.* 21, 21–51.
- Ellefsen, K.J., Hsieh, P.A., Shapiro, A.M., 2002. Crosswell seismic investigation of hydraulically conductive, fractured bedrock near mirror lake, New Hampshire. *J. Appl. Geophys.* 50, 299–317.
- Engelder, T., 2004. Tectonic implications drawn from differences in the surface morphology on two joint sets in the Appalachian Valley and Ridge, Virginia. *Geology* 32, 413–416.
- Fadakar-A, Y., Xu, C., Dowd, P., 2013. Connectivity index and connectivity field towards fluid flow in fracture-based geothermal reservoirs. In: Proceedings of 38 Workshop on Geothermal Reservoir Engineering. Stanford University, Stanford, California, pp. 417–427.
- Huseby, O., Thovert, J., Adler, P., 1997. Geometry and topology of fracture systems. *J. Phys. A Math. Gen.* 30, 1415.
- Im, K., Elsworth, D., Fang, Y., 2018. The influence of preslip sealing on the permeability evolution of fractures and faults. *Geophys. Res. Lett.* 45, 166–175.
- Jeanport, J., Iseppi, M., Adler, P., Genthon, P., Sevin, B., Thovert, J.F., Dewandel, B., Joint, J.L., 2019. Fracture controlled permeability of ultramafic basement aquifers. Inferences from the koniombo massif, New Caledonia. *Eng. Geol.* 256, 67–83.

- Karna, S.K., Sahai, R., et al., 2012. An overview on taguchi method. *Int. J. Eng. Math. Sci.* 1, 1–7.
- Kemeny, J., Post, R., 2003. Estimating three-dimensional rock discontinuity orientation from digital images of fracture traces. *Comput. Geosci.* 29, 65–77.
- Koudina, N., Garcia, R.G., Thovert, J.F., Adler, P., 1998. Permeability of three-dimensional fracture networks. *Phys. Rev. E* 57, 4466.
- Laubach, S.E., 1988. Subsurface fractures and their relationship to stress history in East Texas basin sandstone. *Tectonophysics* 156, 37–49.
- Laubach, S.E., Lander, R., Criscenti, L.J., Anovitz, L.M., Urai, J., Pollyea, R.M., Hooker, J. N., Narr, W., Evans, M.A., Kerisit, S.N., et al., 2019. The role of chemistry in fracture pattern development and opportunities to advance interpretations of geological materials. *Rev. Geophys.* 57, 1065–1111.
- Lei, Q., Latham, J.P., Tsang, C.F., 2017. The use of discrete fracture networks for modelling coupled geomechanical and hydrological behaviour of fractured rocks. *Comput. Geotech.* 85, 151–176.
- Li, X., Zhang, D., Li, S., 2015. A multi-continuum multiple flow mechanism simulator for unconventional oil and gas recovery. *J. Nat. Gas Sci. Eng.* 26, 652–669.
- Maillot, J., Davy, P., Le Goc, R., Darcel, C., De Dreuzy, J.R., 2016. Connectivity, permeability, and channeling in randomly distributed and kinematically defined discrete fracture network models. *Water Resour. Res.* 52, 8526–8545.
- Mourzenko, V.V., Thovert, J.F., Adler, P.M., 2011. Permeability of isotropic and anisotropic fracture networks, from the percolation threshold to very large densities. *Phys. Rev. E* 84, 036307.
- Nur, A., 1982. The origin of tensile fracture lineaments. *J. Struct. Geol.* 4, 31–40.
- Odling, N.E., 1997. Scaling and connectivity of joint systems in sandstones from western Norway. *J. Struct. Geol.* 19, 1257–1271.
- Olson, J.E., 2004. Predicting fracture swarms—the influence of subcritical crack growth and the crack-tip process zone on joint spacing in rock. *Geol. Soc. Spec. Publ.* 231, 73–88.
- Olson, J.E., Laubach, S.E., Lander, R.H., 2009. Natural fracture characterization in tight gas sandstones: integrating mechanics and diagenesis. *AAPG Bull.* 93, 1535–1549.
- Prioul, R., Jocker, J., 2009. Fracture characterization at multiple scales using borehole images, sonic logs, and walkaround vertical seismic profile. *AAPG Bull.* 93, 1503–1516.
- Rijks, E., Jauffred, J., 1991. Attribute extraction: an important application in any detailed 3-d interpretation study. *Lead. Edge* 10, 11–19.
- Robinson, P., 1983. Connectivity of fracture systems—a percolation theory approach. *J. Phys. A Math. Gen.* 16, 605.
- Sanderson, D.J., Nixon, C.W., 2015. The use of topology in fracture network characterization. *J. Struct. Geol.* 72, 55–66.
- Segall, P., Pollard, D.D., 1983. Joint formation in granitic rock of the Sierra Nevada. *Geol. Soc. Am. Bull.* 94, 563–575.
- Thovert, J.F., Mourzenko, V., Adler, P., 2017. Percolation in three-dimensional fracture networks for arbitrary size and shape distributions. *Phys. Rev. E* 95, 042112.
- Ukar, E., Laubach, S.E., Hooker, J.N., 2019. Outcrops as guides to subsurface natural fractures: example from the Nikanassin Formation tight-gas sandstone, Grande Cache, Alberta foothills, Canada. *Mar. Pet. Geol.* 103, 255–275.
- Wang, M., He, J., Yu, J., Pan, N., 2007. Lattice boltzmann modeling of the effective thermal conductivity for fibrous materials. *Int. J. Therm. Sci.* 46, 848–855.
- Watkins, H., Bond, C.E., Healy, D., Butler, R.W., 2015. Appraisal of fracture sampling methods and a new workflow to characterise heterogeneous fracture networks at outcrop. *J. Struct. Geol.* 72, 67–82.
- Whitaker, A.E., Engelder, T., 2005. Characterizing stress fields in the upper crust using joint orientation distributions. *J. Struct. Geol.* 27, 1778–1787.
- Wilt, M., Alumbaugh, D., Morrison, H., Becker, A., Lee, K.H., Deszcz-Pan, M., 1995. Crosswell electromagnetic tomography: system design considerations and field results. *Geophysics* 60, 871–885.
- Xiong, F., Sun, H., Zhang, Q., Wang, Y., Jiang, Q., 2022. Preferential flow in three-dimensional stochastic fracture networks: the effect of topological structure. *Eng. Geol.* 309, 106856.
- Xu, C., Dowd, P., Mardia, K., Fowell, R., 2006. A connectivity index for discrete fracture networks. *Math. Geol.* 38, 611–634.
- Zhu, W., Khirevich, S., Patzek, T., 2018. Percolation properties of stochastic fracture networks in 2d and outcrop fracture maps. In: 80th EAGE Conference and Exhibition 2018. European Association of Geoscientists & Engineers, pp. 1–5.
- Zhu, W., Khirevich, S., Patzek, T.W., 2021. Impact of fracture geometry and topology on the connectivity and flow properties of stochastic fracture networks. *Water Resour. Res.* e2020WR028652.
- Zhu, W., He, X., Li, Y., Lei, G., Santoso, R., Wang, M., 2022a. Impacts of fracture properties on the formation and development of stimulated reservoir volume: a global sensitivity analysis. *J. Pet. Sci. Eng.* 110852.
- Zhu, W., He, X., Santoso, R.K., Lei, G., Patzek, T.W., Wang, M., 2022b. b. Enhancing fracture network characterization: a data-driven, outcrop-based analysis. *Comput. Geotech.* 152, 104997.
- Zhu, W., Khirevich, S., Patzek, T.W., 2022c. Hatchfrac: a fast open-source dfn modeling software. *Comput. Geotech.* 150, 104917.
- Zhu, W., Lei, G., He, X., Yang, Y., Santoso, R.K., Wang, M., 2022d. Can we infer the percolation status of 3d fractured media from 2d outcrops? *Eng. Geol.* 302, 106648.